On dispersion of directional surface gravity waves

Tore Magnus A. Taklo[1], Karsten Trulsen[1]†, Harald E. Krogstad[2] and José Carlos Nieto Borge[3]

[1]Department of Mathematics, University of Oslo, Norway

[2]Department of Mathematical Sciences, Norwegian University of Science and Technology, Norway

[3]Department of Signal Theory and Communications, University of Alcalá, Spain

(Received ; revised ; accepted . - To be entered by editorial office)

Using a nonlinear evolution equation we examine the dependence of the dispersion of directional surface gravity waves on the Benjamin-Feir index (BFI) and crest length. A parameter for describing the deviation between the dispersion of simulated waves and the theoretical linear dispersion relation is proposed. We find that for short crests the magnitude of the deviation parameter is low while for long crests the magnitude is high and depends on the BFI. In the present paper we also consider laboratory data of directional waves from the Marine Research Institute of the Netherlands (MARIN). The MARIN data confirms the simulations for three cases of BFI and crest length.

Key words:

1. Introduction

Linear wave theory is used for a wide range of applications in ocean engineering (Goda 2000; Tucker & Pitt 2001) and assumes that the water surface can be modeled as a linear superposition of non-interacting waves satisfying the linear dispersion relation (LDR). The LDR for surface gravity waves on deep water is

$$\omega = \Omega(k) \equiv (gk)^{1/2} \tag{1.1}$$

where ω is angular frequency, g is acceleration due to gravity, k is wavenumber and Ω is angular frequency according to LDR.

The inversion of marine radar imagery currently relies on linear wave theory as a prerequisite. The analysis of marine radar imagery consists of applying a three-dimensional band-pass filter that supresses those spectral contributions that do not satisfy the LDR (Nieto Borge *et al.* 2004).

Krogstad & Trulsen (2010) simulated unidirectional waves using the nonlinear Schrödinger (NLS) equation and the modified nonlinear Schrödinger (MNLS) equation of Dysthe (1979). From wavenumber-frequency spectra they found that the spectral contribution deviated from LDR due to nonlinear evolution. The deviation was also demonstrated from simulations of unidirectional waves by Gibson & Swan (2006) using the Zakharov (1968) equation and a fully nonlinear wave model by Bateman *et al.* (2001), and also by Houtani *et al.* (2015) using a higher order spectral method.

Taklo *et al.* (2015) reported experiments and simulations, using the Zakharov (1968)

† Email address for correspondence: karstent@math.uio.no

equation, of unidirectional waves. For narrow-banded waves the experiments confirmed the numerical predictions by Gibson & Swan (2006), Krogstad & Trulsen (2010) and Houtani *et al.* (2015). For broad-banded waves the experiments showed that the LDR was satisfied, suggesting validity of linear wave theory. The Zakharov equation was in good agreement with the experiments.

In this paper we examine deviation from LDR for directional waves simulated using the NLS and MNLS equations. We propose a parameter for describing deviation between dispersion of simulated waves and LDR. We parameterize the result as in Gramstad & Trulsen (2007) using BFI and inverse crest length L_c^{-1}.

Our Benjamin-Feir index is defined as

$$\mathrm{BFI} = \frac{\epsilon}{\Delta\omega/\omega_p} \tag{1.2}$$

where ϵ is wave steepness, and $\Delta\omega$ and ω_p are bandwidth and peak frequency of frequency spectrum, respectively (Alber 1978; Alber & Saffman 1978; Crawford *et al.* 1980; Onorato *et al.* 2001; Janssen 2003). The BFI will be further specified below. Our non-dimensional crest length is defined as

$$L_c = \frac{k_p}{\Delta k_y} \tag{1.3}$$

where k_p is peak wavenumber, the peak wave vector is in the x-direction, and Δk_y is transversal bandwidth in the y-direction.

A presentation of numerical simulations is given in §2 and numerical results are presented in §3. The MARIN data are considered in §4. A discussion is given in §5 and concluding remarks are given in §6.

2. Numerical simulations

Simulations were performed with the NLS equation and the MNLS equation of Dysthe (1979). These employ an expression for surface elevation on the form

$$\eta = \bar{\eta} + \frac{1}{2}\Big(B\mathrm{e}^{\mathrm{i}\chi} + B_2\mathrm{e}^{2\mathrm{i}\chi} + B_3\mathrm{e}^{3\mathrm{i}\chi} + ... + \mathrm{c.c.}\Big) \tag{2.1}$$

where $\mathrm{i}=\sqrt{-1}$ is the imaginary unit, c.c. denotes complex conjugate and B is the first harmonic complex amplitude of the waves. We let the phase function be $\chi = (\mathbf{k}_p\cdot\mathbf{x}-\omega_p t)$ where $\mathbf{x}=(x,y)$ is the horizontal position vector, t is time, $\mathbf{k}_p=(k_p,0)$ is the peak wave vector and $\omega_p = \Omega(\mathbf{k}_p) = (g|\mathbf{k}_p|)^{1/2}$ is the LDR peak frequency.

The zeroth harmonic, $\bar{\eta}$, and the complex amplitudes of the higher harmonics, $B_2, B_3, ...$, can be expressed in terms of B, see Toffoli *et al.* (2010) equation (3.4). We shall only be concerned about the spectral contribution of η close to the peak k_p and ω_p. For this reason we only consider the contribution from B for reconstruction of the surface elevation in (2.1).

The MNLS equation is

$$\frac{\partial B}{\partial t} + \mathcal{L}B + \frac{\mathrm{i}\omega_p {k_p}^2}{2}|B|^2B + \frac{3\omega_p k_p}{2}|B|^2\frac{\partial B}{\partial x} + \frac{\omega_p k_p}{4}B^2\frac{\partial B^*}{\partial x} + \mathrm{i}k_p\frac{\partial\bar{\phi}}{\partial x}\bigg|_{z=0}B = 0 \tag{2.2}$$

where $*$ denotes complex conjugate.

The induced mean flow $\bar{\phi}$ is governed by

$$\frac{\partial\bar{\phi}}{\partial z} = \frac{\omega_p}{2}\frac{\partial|B|^2}{\partial x} \quad \text{at} \quad z = 0, \tag{2.3}$$

$$\nabla^2\bar{\phi} = 0 \quad \text{for} \quad -\infty < z < 0, \tag{2.4}$$

$$\frac{\partial\bar{\phi}}{\partial z} = 0 \quad \text{at} \quad z \to -\infty \tag{2.5}$$

where $\nabla = (\partial/\partial x, \partial/\partial y, \partial/\partial z)$.

The differential operator $\mathcal{L}$ accounts for linear dispersion. Following Trulsen *et al.* (2000) it can be written in exact form

$$\mathcal{L} = \mathrm{i}\left(\left(g\left(\left(k_p - \mathrm{i}\frac{\partial}{\partial x}\right)^2 - \frac{\partial^2}{\partial y^2}\right)^{1/2}\right)^{1/2} - \left(gk_p\right)^{1/2}\right). \tag{2.6}$$

By considering the first three terms of (2.2) the NLS equation is recovered.

Most of the simulations are initialized with a Gaussian wave vector spectrum

$$\Psi(\mathbf{k}) = \frac{a_c^2}{4\pi\sigma_x\sigma_y k_p^2}\exp\left[-\frac{1}{2}\left(\left(\frac{(k_x - k_p)}{\sigma_x k_p}\right)^2 + \left(\frac{k_y}{\sigma_y k_p}\right)^2\right)\right] \tag{2.7}$$

symmetric around the peak wave vector $\mathbf{k}_p = (k_p, 0)$ where $\mathbf{k} = (k_x, k_y)$ is the horizontal wave vector and σ_x and σ_y are non-dimensional longitudinal and transversal bandwidths, respectively. The characteristic amplitude of the surface elevation η is $a_c = (2\langle\eta^2\rangle)^{1/2}$ where $\langle\cdot\rangle$ denotes statistical averaging. The spectrum fulfils the normalization criterion

$$\int\int \Psi(\mathbf{k})\mathrm{d}k_x\mathrm{d}k_y = \frac{a_c^2}{2}. \tag{2.8}$$

The average steepness is $\epsilon = a_c k_p$. We perform simulations with $\epsilon = 0.04$, 0.06, 0.08 and 0.10. The highest steepness $\epsilon = 0.10$ corresponds to the average maximum steepness observed in the ocean as demonstrated by figure 2 in Socquet-Juglard *et al.* (2005).

For comparison with the MARIN laboratory data we perform simulations initialized with a JONSWAP spectrum,

$$E(\omega,\theta) = \frac{\alpha g^2}{\omega^5}\exp\left[-\frac{5}{4}\left(\frac{\omega_p}{\omega}\right)^4\right]\gamma^{\exp\left[-\frac{(\omega-\omega_p)^2}{2\sigma^2\omega_p^2}\right]}D(\theta) \tag{2.9}$$

with Phillips factor α, peak enhancement factor $\gamma = 3.3$ and

$$\sigma = \begin{cases} 0.07 & \omega \leqslant \omega_p \\ 0.09 & \omega > \omega_p. \end{cases} \tag{2.10}$$

The directional spreading used for initialization was

$$D(\theta) = \frac{\Gamma(\frac{N}{2}+1)}{\sqrt{\pi}\Gamma(\frac{N}{2}+\frac{1}{2})}\cos^N\theta \quad \text{for} \quad |\theta| \leqslant \pi/2 \tag{2.11}$$

where Γ is the Gamma function, N is a spreading parameter and θ is the direction. Simanesew *et al.* (2016) showed that this initially frequency-independent directional spreading evolved into a frequency-dependent directional spreading when simulated with the MNLS equation.

For initialization of simulations the spectrum (2.9) is transformed to a wave vector

spectrum

$$\Psi(\mathbf{k}) = E(\Omega(\mathbf{k}), \theta)k^{-1}\frac{\mathrm{d}\Omega}{\mathrm{d}k} \tag{2.12}$$

where $\mathbf{k} = (k\cos\theta, k\sin\theta)$ and $\omega = \Omega(\mathbf{k})$ according to the LDR.

To solve the model equations numerically we use the method described by Lo & Mei (1985, 1987) with periodic boundary conditions in both horizontal directions. In order to employ the narrow-banded models we truncate the spectra within $|\mathbf{k} - \mathbf{k}_p| \leqslant k_p$ around the peak $\mathbf{k}_p$. We let x and y be the longitudinal and transversal coordinates, respectively. The computational domain extends over 70 peak wavelengths λ_p in both the x and y-directions. For directional waves we use a uniform grid of $N_x \times N_y = 512 \times 512$ nodes. For unidirectional waves we use a uniform grid of $N_x = 512$ nodes along the x-axis. In time we let the waves evolve for 150 peak periods T_p.

We perform a number of unidirectional and directional simulations with the Gaussian spectrum (2.7) for steepnesses $\epsilon = 0.04$, 0.06, 0.08 and 0.10. For all steepnesses we perform simulations for longitudinal bandwidth σ_x between 0.07 and 0.49 and transversal bandwidth σ_y between 0 and 0.50, in steps of 0.02. The number of simulations is $4{\times}22{\times}26{=}2288$. In addition we perform 3 simulations with the JONSWAP spectrum (2.9)–(2.12) for comparison with the MARIN laboratory data.

From surface elevations $\eta(x, y, t)$, the (k_x, k_y, ω)-spectra are obtained by discrete Fourier transform. In the following we present (k, ω)-spectra obtained by transforming (k_x, k_y, ω)-spectra from Cartesian to polar coordinates using the relations $k_x = k\cos\theta$ and $k_y = k\sin\theta$ and by integrating over θ.

To describe deviation between dispersion of simulated waves and LDR we propose the following deviation parameter

$$\delta = \frac{\int\int \Big(\omega - \Omega(k)\Big) S_1(k, \omega)\mathrm{d}\omega\mathrm{d}k}{\omega_p \int\int S_1(k, \omega)\mathrm{d}\omega\mathrm{d}k}. \tag{2.13}$$

In (2.13), $\Omega(k)$ is given by (1.1), S_1 is the (k, ω)-spectrum from the simulations and ω_p is the peak frequency of the initial spectrum (2.7). The integrals are evaluated over the spectral domain within $|\mathbf{k} - \mathbf{k}_p| \leqslant k_p$. Equation (2.13) can be regarded as a normalised first moment of deviation from LDR.

For comparison of simulated waves with LDR we compute the root mean square (RMS) wavenumber

$$k_{\mathrm{RMS}}(\omega) = \left(\frac{\int\int k^2 S_2(k_x, k_y, \omega)\mathrm{d}k_x\mathrm{d}k_y}{\int\int S_2(k_x, k_y, \omega)\mathrm{d}k_x\mathrm{d}k_y} \right)^{1/2} \tag{2.14}$$

corresponding to each frequency ω where $k = (k_x^2 + k_y^2)^{1/2}$ and S_2 is the (k_x, k_y, ω)-spectrum from the simulations.

The bandwidths $\Delta\omega$ and Δk_y used for BFI (1.2) and L_c (1.3), respectively, were determined from the initial spectrum (2.7) using half-width at half-peak (HWHP). The bandwidth $\Delta\omega$ was found by rewriting (2.7) to a k-spectrum using polar coordinates and $\Delta\omega$ was computed from $\Delta\omega = \omega_p((1 + \Delta k/k_p)^{1/2} - 1)$ where Δk is HWHP of the k-spectrum. The bandwidth Δk_y was computed from HWHP of the k_y-spectrum corresponding to (2.7).

While Δk_y depends on σ_y only, $\Delta\omega$ depends on both σ_x and σ_y. As a consequence the

data of BFI and L_c are nonuniformly distributed given a uniform grid for σ_x and σ_y. In the following we present the scalar field of δ (2.13) as a function of BFI and inverse crest length L_c^{-1}. In order to plot $\delta(\mathrm{BFI}, L_c^{-1})$ the scalar field is fitted to a uniform grid by cubic interpolation. As a consequence of the grid the upper right corners of the contour plots of δ are empty, see figure 5.

For the highest steepness $\epsilon = 0.10$, BFI ranges from 0.39 to 2.63. For the lowest steepness $\epsilon = 0.04$, BFI ranges from 0.15 to 1.05. For σ_y between 0 and 0.50, L_c ranges from $1.70\lambda_p$ up to unidirectional waves. Correspondingly, L_c^{-1} ranges from 0 to 0.59.

There have been recent attempts to combine BFI and directionality into a single directional BFI (Waseda *et al.* 2009; Mori *et al.* 2011; Xiao *et al.* 2013) with the purpose of parameterizing kurtosis and rogue wave occurence. Our purpose is different, to parameterize the deviation from the LDR, however, by comparing our results of δ to the directional BFI of Mori *et al.* (2011) we find that it could be a suitable parameter for identifying the deviation.

3. Numerical results

Figure 1 shows (k, ω)-spectra from directional simulations with the highest steepness $\epsilon = 0.10$ and the narrowest initial bandwidths $\sigma_x = 0.07$ and $\sigma_y = 0.02$. Colours show spectral energy density in decibel (dB) relative to the peak. White dashed curves show LDR, $\Omega(k)$, from (1.1). Upper and lower panes show spectral evolution with regard to the NLS and MNLS equations, respectively. Left panes show the (k, ω)-spectra during the first fifty peak periods $t/T_p \in [0, 50]$. Center panes show $t/T_p \in [50, 100]$ and right panes show $t/T_p \in [100, 150]$.

Figure 1 shows the qualitative difference between spectral evolution for the NLS and MNLS equations. For the NLS equation, the spectral energy density grows symmetrically around the peak while for the MNLS equation it grows asymmetrically to wavenumbers and frequencies above peak.

Within $t/T_p \in [0, 50]$ the waves quickly evolve into a state where spectral energy density deviates from the LDR. The white dotted curves show the RMS wavenumber, $k_{\mathrm{RMS}}(\omega)$ from (2.14), which confirms the deviation. For the NLS equation the deviation is pronounced both above and below peak while for the MNLS equation the deviation is pronounced only above peak. Above peak the MNLS equation contributes to a more pronounced deviation than the NLS equation during the time considered. Within $t/T_p \in [100, 150]$ the spectral energy density is spread out to a rather broad distribution and starts to relax toward the LDR.

We performed simulations over longer times up to $200T_p$ which revealed that the directional waves eventually reach a quasi-stationary state with relaxation toward the LDR. Our narrow-banded unidirectional waves show deviation during the entire time up to $200T_p$. The unidirectional waves do not reach a quasi-stationary state with relaxation toward the LDR. Thus a qualitative difference between directional and unidirectional wave propagation is observed. Qualitative difference was also observed by Gramstad & Trulsen (2007).

Figure 2 shows spectral evolution from directional simulations of the MNLS equation for steepnesses $\epsilon = 0.04$, 0.06 and 0.08 and the narrowest initial bandwidths. Upper, middle and lower panes show spectral evolution for $\epsilon = 0.04$, 0.06 and 0.08, respectively. The waves evolve on Benjamin-Feir (BF) timescale $(\epsilon^2\omega_p)^{-1}$ thus for different ϵ ranging from 0.04 to 0.10 characteristic time scales differ by approximately one order of magnitude. For $\epsilon = 0.04$, 0.06, 0.08 and 0.10, BF time scale covers 100, 44, 25 and $16T_p$, respectively. Figure 2 and the lower panes of figure 1 show that the occurence of deviation depends

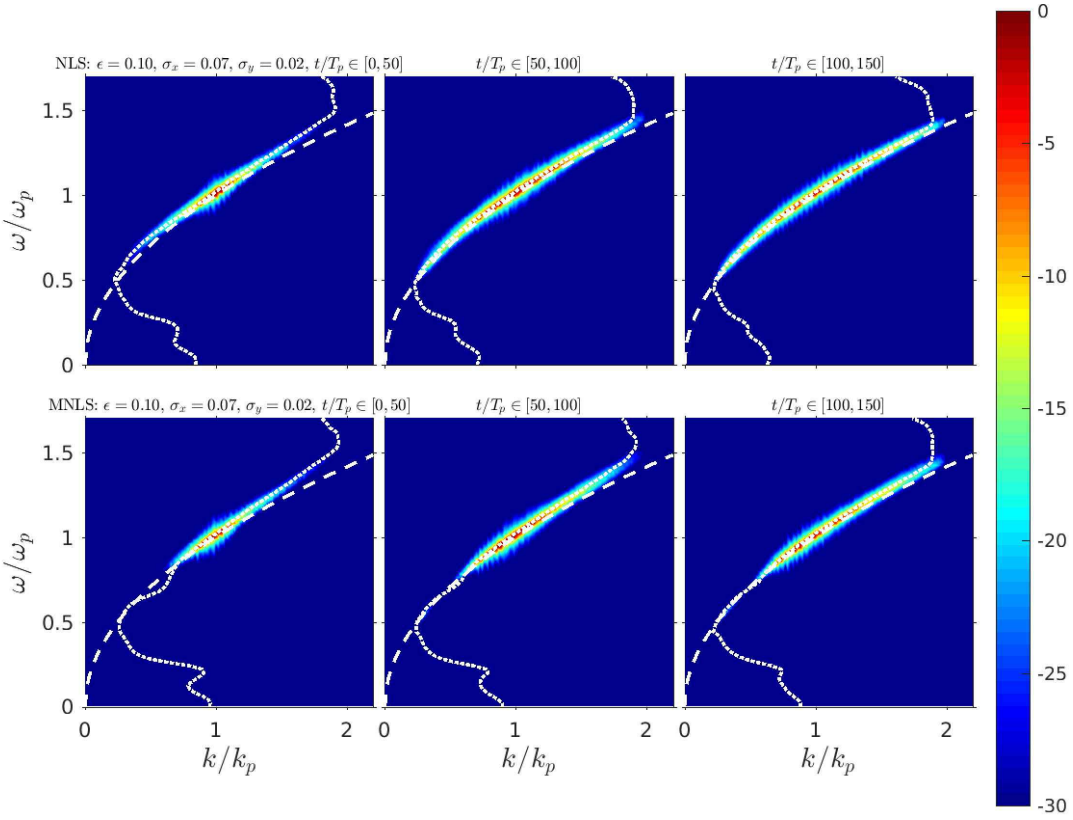

FIGURE 1. Evolution of (k, ω)-spectra of directional wave field with $\epsilon = 0.10$ and $\sigma_x = 0.07$ and $\sigma_y = 0.02$. Colours: Spectral energy density in dB. White dashed curves: LDR $\Omega(k)$ from (1.1). White dotted curves: RMS wavenumber $k_{\mathrm{RMS}}(\omega)$ from (2.14). First column, $t/T_p \in [0, 50]$; second column, $t/T_p \in [50, 100]$ and third column, $t/T_p \in [100, 150]$. Upper panes: NLS equation. Lower panes: MNLS equation.

on the characteristic time scales. For waves with high steepness deviation occurs, and relaxes toward LDR, sooner than for waves with lower steepness.

Figure 3 shows a selection of (k, ω)-spectra of directional waves simulated with the MNLS equation with $\epsilon = 0.10$ and different combinations of initial bandwidths σ_x and σ_y given in the titles of the panes. The spectral estimates are taken from $t/T_p \in [100, 150]$ to observe occurence of deviation farthest from initialization. The upper left pane is identical to the lower right pane of figure 1. First column corresponds to $\sigma_x = 0.07$, second column $\sigma_x = 0.23$ and third column $\sigma_x = 0.49$. First row corresponds to $\sigma_y = 0.02$, second row $\sigma_y = 0.26$ and third row $\sigma_y = 0.50$.

From figure 3 it is observed that the occurence of deviation depends on the initial bandwidths. For combinations of broad bandwidths corresponding to the four panes in the lower right corner of figure 3, deviation does not occur. To first order in magnitude, i.e. dB>-10, and within the spectral radius of the simulations the spectral distribution resembles the shape of the LDR. Nevertheless, above peak the spectral distribution is

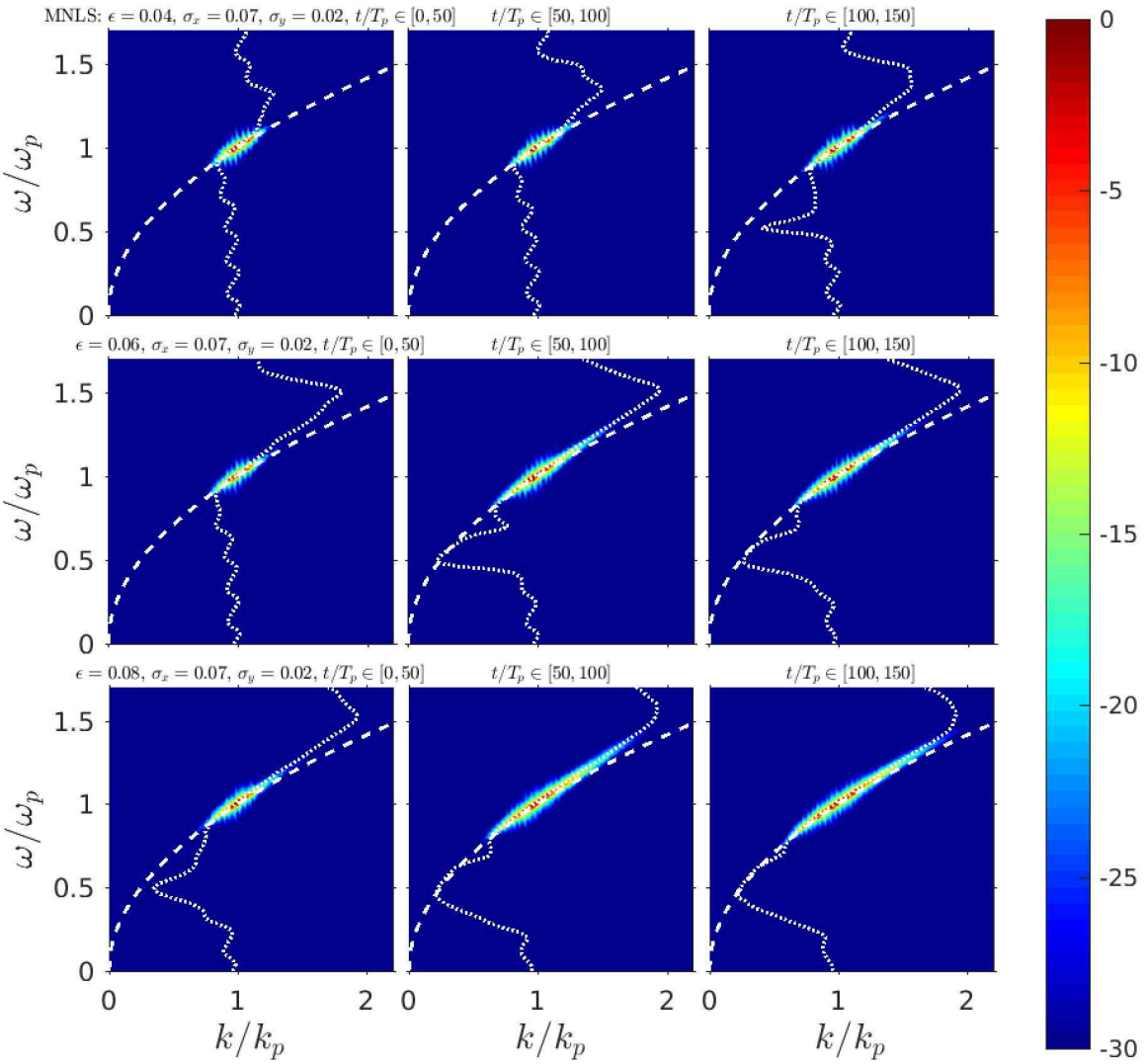

FIGURE 2. Evolution of (k, ω)-spectra of directional wave fields simulated using the MNLS equation with different ϵ and $\sigma_x = 0.07$ and $\sigma_y = 0.02$. Colours: Spectral energy density in dB. White dashed curves: LDR $\Omega(k)$ from (1.1). White dotted curves: RMS wavenumber $k_{\mathrm{RMS}}(\omega)$ from (2.14). First column, $t/T_p \in [0, 50]$; second column, $t/T_p \in [50, 100]$ and third column, $t/T_p \in [100, 150]$. Upper panes, $\epsilon = 0.04$; middle panes, $\epsilon = 0.06$ and lower panes, $\epsilon = 0.08$.

shifted slightly toward wavenumbers and frequencies above LDR. This will be further explained below.

The simulations with $\epsilon = 0.04$, 0.06 and 0.08 show qualitatively similar results to those observed in figure 3 with occurence of deviation for combinations of narrow bandwidths. For $\epsilon = 0.08$ the shift above peak is observed for combinations of broad bandwidths

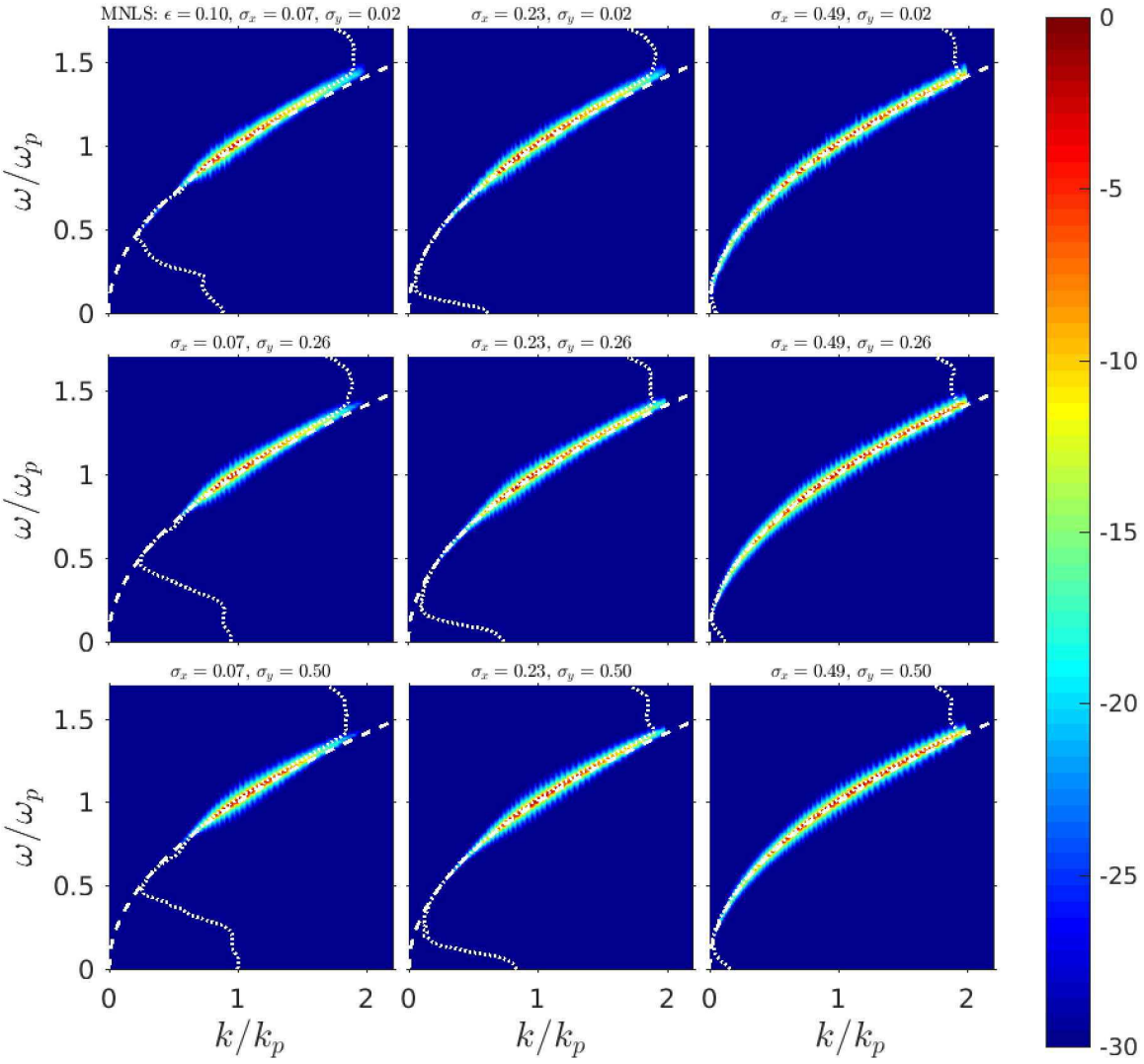

FIGURE 3. (k, ω)-spectra of directional wave fields from time interval $t/T_p \in [100, 150]$ simulated using the MNLS equation with $\epsilon = 0.10$ and combinations of different σ_x and σ_y given in the title of the panes. Colours: Spectral energy density in dB. Colour bar in dB. White dashed curves: LDR $\Omega(k)$ from (1.1). White dotted curves: RMS wavenumber k_{RMS} from (2.14).

similarly to that observed for $\epsilon = 0.10$ while for $\epsilon = 0.06$ and 0.04 the shift is less evident.

Figure 4 shows (k, ω)-spectra of $\epsilon = 0.10$ and 0.04 and broadest initial bandwidths $\sigma_x = 0.49$ and $\sigma_y = 0.50$. Left pane corresponds to lower right pane of figure 3. For $\epsilon = 0.10$ it is observed that the spectral distribution is shifted toward wavenumbers and frequencies above LDR. For $\epsilon = 0.04$ the shift is less evident. The RMS wavenumber confirms the observation. Thus when the steepness is high, nonlinear evolution can cause a shift

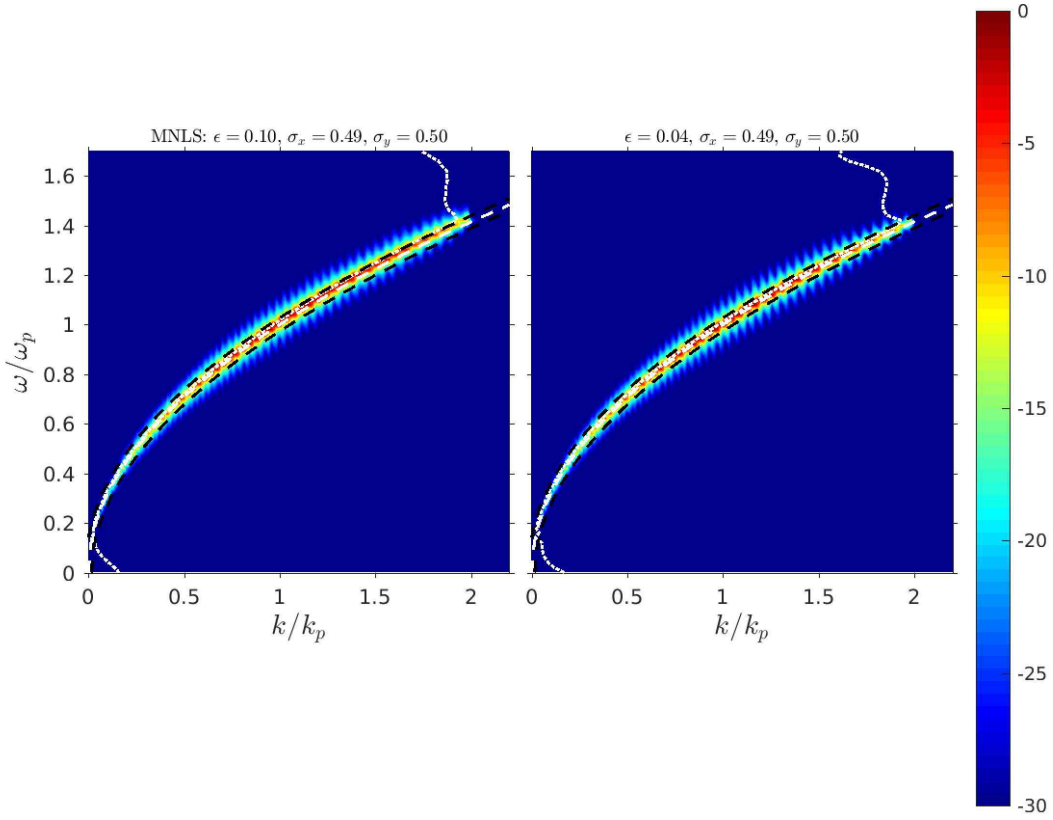

FIGURE 4. (k, ω)-spectra of directional wave fields from time interval $t/T_p \in [100, 150]$ simulated using the MNLS equation with $\epsilon = 0.10$ and $\epsilon = 0.04$ and combinations of the broadest bandwidths σ_x and σ_y given in the title of the panes. Colours: Spectral energy density in dB. Colour bar in dB as in figure 3. White dashed curves: LDR $\Omega(k)$ from (1.1). White dotted curves: RMS wavenumber k_{RMS} from (2.14). Black dashed curves: Radar filter $\omega(k \pm \Delta k) \pm \Delta\omega$ as a function of k where Δk and $\Delta\omega$ are the resolutions along the wavenumber and frequency axes given by the discrete Fourier transform.

from the LDR for broad-banded waves. The black dashed curves show $\omega(k \pm \Delta k) \pm \Delta\omega$ as a function of k where Δk and $\Delta\omega$ are the resolutions along the wavenumber and frequency axes given by the discrete Fourier transform. These curves are commonly used as a criterion for the interpretation of marine radar images to filter out those spectral contributions that do not satisfy the LDR (Nieto Borge *et al.* 2004). For $\epsilon = 0.10$ the spectral energy density is distributed along $\omega(k+\Delta k)+\Delta\omega$ above LDR while for $\epsilon = 0.04$ the spectral energy density is distributed below $\omega(k + \Delta k) + \Delta\omega$ and closer to LDR.

Figure 5 shows δ (2.13) as a function of BFI and L_c^{-1} for 2288 simulations of the MNLS equation with $\epsilon = 0.04$, 0.06, 0.08 and 0.10. The spectral estimates for δ are taken from $t/T_p \in [100, 150]$. Note that the BFI axes are different due to the different steepnesses involved. Symbols show the locations of spectra with bandwidths corresponding to diagonal panes of figure 3. Triangle symbols show the locations of data points corresponding to BFI and L_c^{-1} estimated from the MARIN data and will be further explained in §4.

For all steepnesses we find that the deviation from the LDR is most pronounced when

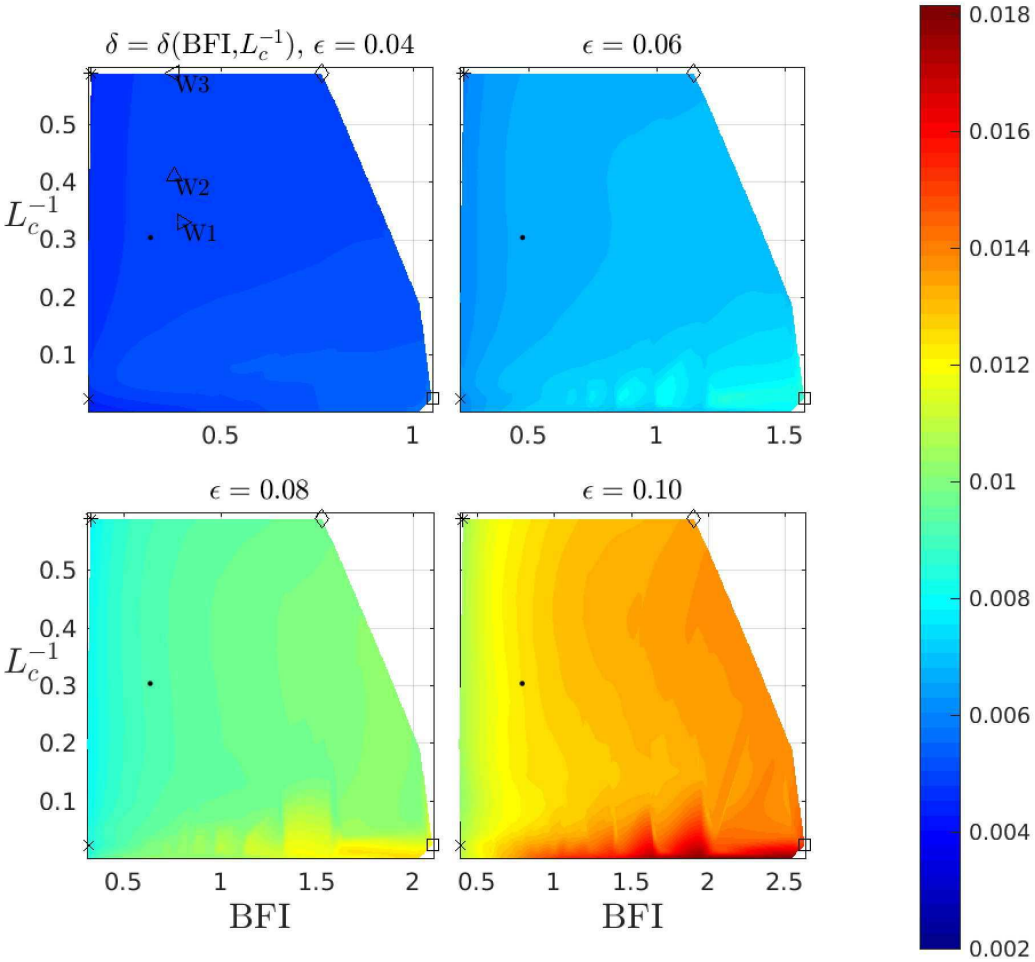

FIGURE 5. Colours: Deviation parameter δ (2.13) as function of BFI and inverse crest length L_c^{-1} for $\epsilon = 0.04$, 0.06, 0.08 and 0.10. Colour bar: Magnitude of δ. Symbols showing location of data points corresponding to the initial bandwidths of the (k, ω)-spectra shown in the diagonal panes of figures 3: $\square$, $\sigma_x = 0.07$ and $\sigma_y = 0.02$; $\diamond$, $\sigma_x = 0.07$ and $\sigma_y = 0.50$; $\times$, $\sigma_x = 0.49$ and $\sigma_y = 0.02$; $*$, $\sigma_x = 0.49$ and $\sigma_y = 0.50$ and $\bullet$, $\sigma_x = 0.23$ and $\sigma_y = 0.26$. Symbols showing location of data points corresponding to the BFI and inverse crest lengths L_c^{-1} estimated from MARIN data: $\triangleright$, W1; $\triangle$, W2; $\triangleleft$, W3.

the BFI is high and crests are long, and the deviation increases when the BFI increases. The highest magnitudes of δ were found for $\epsilon = 0.10$. In particular, the highest magnitude for δ was found for the highest BFI given for unidirectional waves with $\epsilon = 0.10$. For $\epsilon = 0.10$ there is a sharp transition between high and low magnitudes of δ when crests are long and the BFI is high. Also, the magnitude of δ is significantly higher for $\epsilon = 0.10$ compared to other steepnesses and covers a wider range relative to the lowest steepness.

Another feature observed from figure 5 is oscillations of isolines of δ for high BFI and long crests seen for $\epsilon = 0.06$, 0.08 and 0.10. This is a consequence of nonuniformly

distributed data of BFI and L_c^{-1} discussed at the end of §2. The peaks of oscillations appear at locations of the nonuniformly distributed data of BFI and L_c^{-1}. Nevertheless, the choice for BFI and L_c^{-1} should be sufficient to capture the essential result of deviation for high BFI and long crests.

Instead of the Gaussian initial spectrum (2.7) we could have used a JONSWAP spectrum (2.12). Gramstad & Trulsen (2007) showed in their figure 3 that with a JONSWAP spectrum it is not possible to obtain BFI as high as those obtained from the Gaussian spectrum here. We have used the Gaussian spectrum in order to examine a wider range of BFI.

4. Laboratory data

The laboratory data were collected from MARIN's Seakeeping and Manoeuvring Basin. The basin is 170 m × 40 m and the water depth was $h = 5$ m. Waves were generated along one of the short side-walls of the basin. The basin was equiped with flap type wave makers, adjustable wave absorbing beaches and a carriage consisting of a 10×10 array of resistance type wave probes. The probes consisted of thin wires. The sampling rate of the probes was 100 Hz. The 10×10 array was fixed to a carriage which could be positioned at any location in the basin. The wave fields were repeatable, see Naaijen *et al.* (2009). Spatio-temporal measurements were achieved by positioning the carriage at different locations in repetitions of the same wave field. We refer to this collection of spatio-temporal measurements as the synthetic array.

Three directional wave fields were generated. We name the wave fields W1, W2 and W3. Figure 6 shows the locations L1–L12 of the 10×10 array in the basin. The main wave direction was in the x-direction of the basin. The distance from the wave makers to the center of location L12 was 7.0 m. The length of the synthetic array in the x and y-directions was 25.6 m and 26.8 m, respectively. In the following we consider measurements from two sub-arrays, named sub-array 1 and 2, indicated in figure 6. Sub-array 1 consisted of measurements from locations L1, L2, L3, L4, L8 and L12 along the main wave direction. Sub-array 2 consisted of measurements from locations L5–L11 perpendicular to the main wave direction. For wave fields W1 and W3 only measurements from locations L7–L9 were available perpendicular to the main wave direction.

The MARIN wave fields were initialized with a JONSWAP spectrum (2.9)–(2.12) with different directional spreading. Simanesew *et al.* (2016) analyzed these wave fields with respect to directional spreading and found that even though the waves were generated with frequency-independent directional spreading they naturally evolved into frequency-dependent directional spreading similar to that observed in the ocean.

Table 1 shows initial parameters for W1, W2 and W3 estimated from sub-array 2. The location of sub-array 2 is close to the wave makers and is suitable for obtaining an estimate of initial parameters. From directional data of sub-array 2 we computed (k_y, ω)-spectra. The (k_y, ω)-spectra were obtained from uniform discrete Fourier transform of time series and nonuniform discrete Fourier transform (Fessler & Sutton 2003) of data along the y-axis. In order to use directional data from all probes in sub-array 2 we computed a collection of $(k_y, \omega; x)$-spectra from 10 extracts along the y-direction and averaged over x to obtain the (k_y, ω)-spectrum. Extract number 1 is shown in figure 6 and extracts number 2–10 are those that follow along the x-direction.

The initial peak frequencies ω_p of W1, W2 and W3 were estimated from ω-spectra obtained from projection of (k_y, ω)-spectra onto the ω-axis, and peak wavenumbers $k_p = \omega_p^2/g$ were then obtained from LDR. The peak frequencies ω_p and wavenumbers k_p are given in table 1. For W1 the synthetic array covered about $16\lambda_p$ along the main

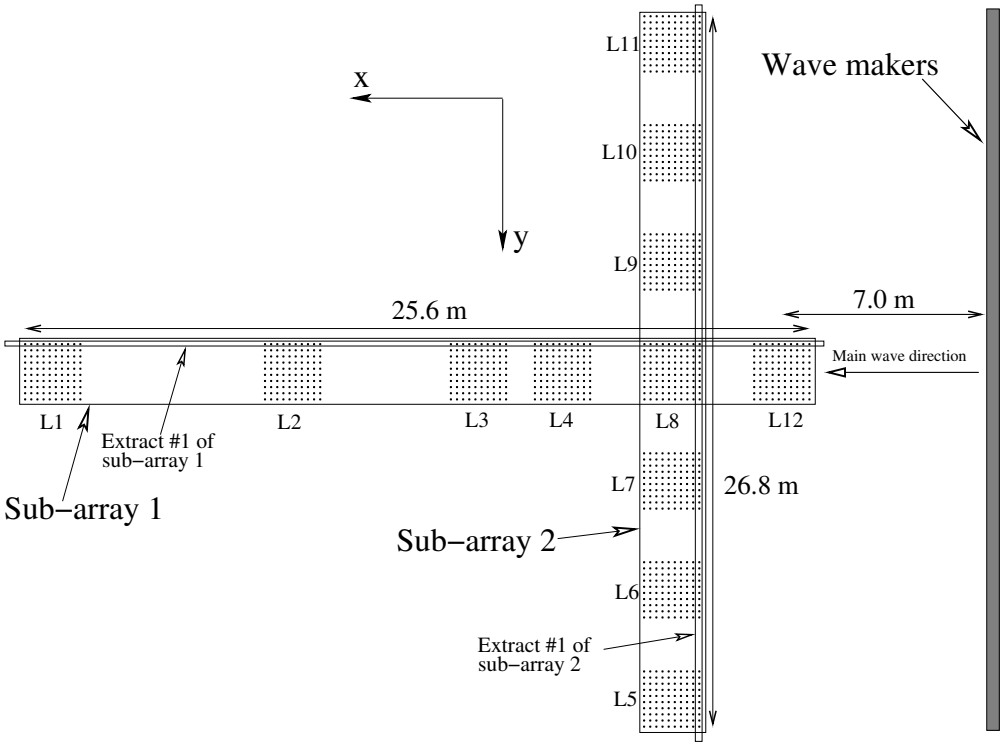

FIGURE 6. Top-view of the MARIN basin showing actual ratio between width and length of the synthetic array.

wave direction and $17\lambda_p$ perpendicular to the main wave direction. For W2 and W3 the synthetic array covered about $15\lambda_p$ along the main wave direction and about $16\lambda_p$ perpendicular to the main wave direction. The non-dimensional water depth $k_p h$ was about 20 for W1 and 19 for W2 and W3. The wave fields were generated for $579T_p$. The first $100T_p$ and last $429T_p$ were removed and the remaining $50T_p$ were used for spectral estimates. The spectra were ensemble averaged by 2 non-overlapping intervals of surface elevation of length $25T_p$ collected from total time interval of $50T_p$. The time intervals of about $25T_p$ were smoothed by 10 iterations of a 3-point moving average.

Peak frequencies ω_p were also estimated from ω-spectra obtained from time series at each of the 10×60 probes in sub-array 1. These peak frequencies were similar to those given in table 1 and relatively constant along the basin.

From table 1 we notice that W1, W2 and W3 have identical steepness, practically similar BFI, and noticeably different crest length. The data points of BFI and inverse crest length L_c^{-1} from MARIN data are plotted in figure 5 for the simulations with steepness $\epsilon = 0.04$ in §3. The data points are situated away from highest values of δ, indicating that deviation due to nonlinear evolution should not be observable from the MARIN data. Figure 5 is obtained from simulations of Gaussian spectra while the MARIN data had JONSWAP spectra, nevertheless the comparison should be reasonable for the relatively low BFI and short crests involved.

The steepness was also estimated from time series at each of the 10×60 probes in sub-array 1 and was similar to the steepness estimated from sub-array 2 given in table 1. Thus the wave fields were not attenuated along the main wave direction.

Wave field	ω_p [s^{-1}]	T_p [s]	k_p [m^{-1}]	λ_p [m]	ϵ [-]	$\Delta\omega/\omega_p$ [-]	BFI [-]	L_c [-]	N [-]
W1	6.29	1.00	4.04	1.56	0.04	0.100	0.40	3.06	17
W2	6.04	1.04	3.72	1.69	0.04	0.104	0.38	2.42	11
W3	6.04	1.04	3.72	1.69	0.04	0.104	0.38	1.69	5

TABLE 1. Parameters from the MARIN wave fields estimated from sub-array 2 in the basin: ω_p, peak frequency; T_p, peak period; k_p, peak wavenumber; λ_p, peak wavelength; ϵ, steepness; $\Delta\omega/\omega_p$, HWHP frequency bandwidth; BFI, Benjamin-Feir index; L_c, crest length and N, spreading parameter given for MNLS simulations for initial spectrum (2.9).

The left panes of figure 7 show (k_x, ω)-spectra of W1, W2 and W3 obtained from sub-array 1. In order to use the directional data from all probes in sub-array 1 we computed a collection of $(k_x, \omega; y)$-spectra from 10 extracts along the x-direction in the basin and averaged over y to obtain the (k_x, ω)-spectrum. Extract number 1 is shown in figure 6 and extracts number 2–10 are those that follow along the y-direction. The (k_x, ω)-spectra were obtained by uniform discrete Fourier transform of the time series and nonuniform discrete Fourier transform (Fessler & Sutton 2003) of the data along the x-axis.

The axes of the left panes of figure 7 are normalized by the peak frequencies ω_p estimated from the ω-spectra obtained from projection of the (k_x, ω)-spectra of W1, W2 and W3 onto the ω-axis, and the peak wavenumbers $k_p = \omega_p^2/g$ from LDR. The peak frequencies ω_p and wavenumbers k_p were similar to those given in table 1.

In order to compare distributions of (k_x, ω)-spectra with linear wave theory we compute

$$\lim_{k_y \to 0} \Omega(k) = (g|k_x|)^{1/2} \tag{4.1}$$

i.e. LDR (1.1) in the limit that $k_y = 0$. In figure 7, the white dashed curves show (4.1).

The (k_x, ω)-spectra from the MARIN data reveal contributions around (4.1) and the peaks of the spectra are in accordance with (4.1). When waves satisfying LDR are projected onto the (k_x, ω)-plane the curve (4.1) should be a lower bound for contributions in the projected spectral plane. There is no indication of deviation from LDR for the MARIN spectra. Additional distributions are seen away from peak. These are caused by aliasing as a consequence of gaps between the measurement locations in the basin. The white dotted curves show the RMS wavenumber k_{RMS} (2.14). The RMS wavenumber is distributed close to peak but as a consequence of aliasing the estimate of the RMS wavenumber is slightly inaccurate.

The right panes of figure 7 show (k_x, ω)-spectra obtained from simulations of the MNLS equation. The simulations were initialized with the JONSWAP spectrum (2.9)–(2.12) with α chosen such that $\epsilon = 0.04$ identical to the steepness of the MARIN wave fields. The directional spreading was determined by the spreading parameter N given for the spreading function $D(\theta)$ (2.11). The spreading parameters N that corresponded to L_c of the MARIN wave fields were used for simulations and are given in table 1.

The MARIN wave fields were simulated on a computational domain extending over $70\lambda_p$ in both the x and y-directions. A uniform grid of $N_x \times N_y = 512 \times 512$ nodes was used. From this domain, sub-domains with spatial coverage identical to that of MARIN sub-array 1 were selected i.e. $16\lambda_p$ for W1 and $15\lambda_p$ for W2 and W3 along main wave direction. Within the sub-domains the nodes corresponding to gaps between measurement locations in sub-array 1 were removed in order to simulate the nonuniform spatial coverage. The simulated wave fields evolved for $150T_p$ and as for the MARIN wave fields we removed the first $100T_p$ and used the next $50T_p$ for spectral estimates.

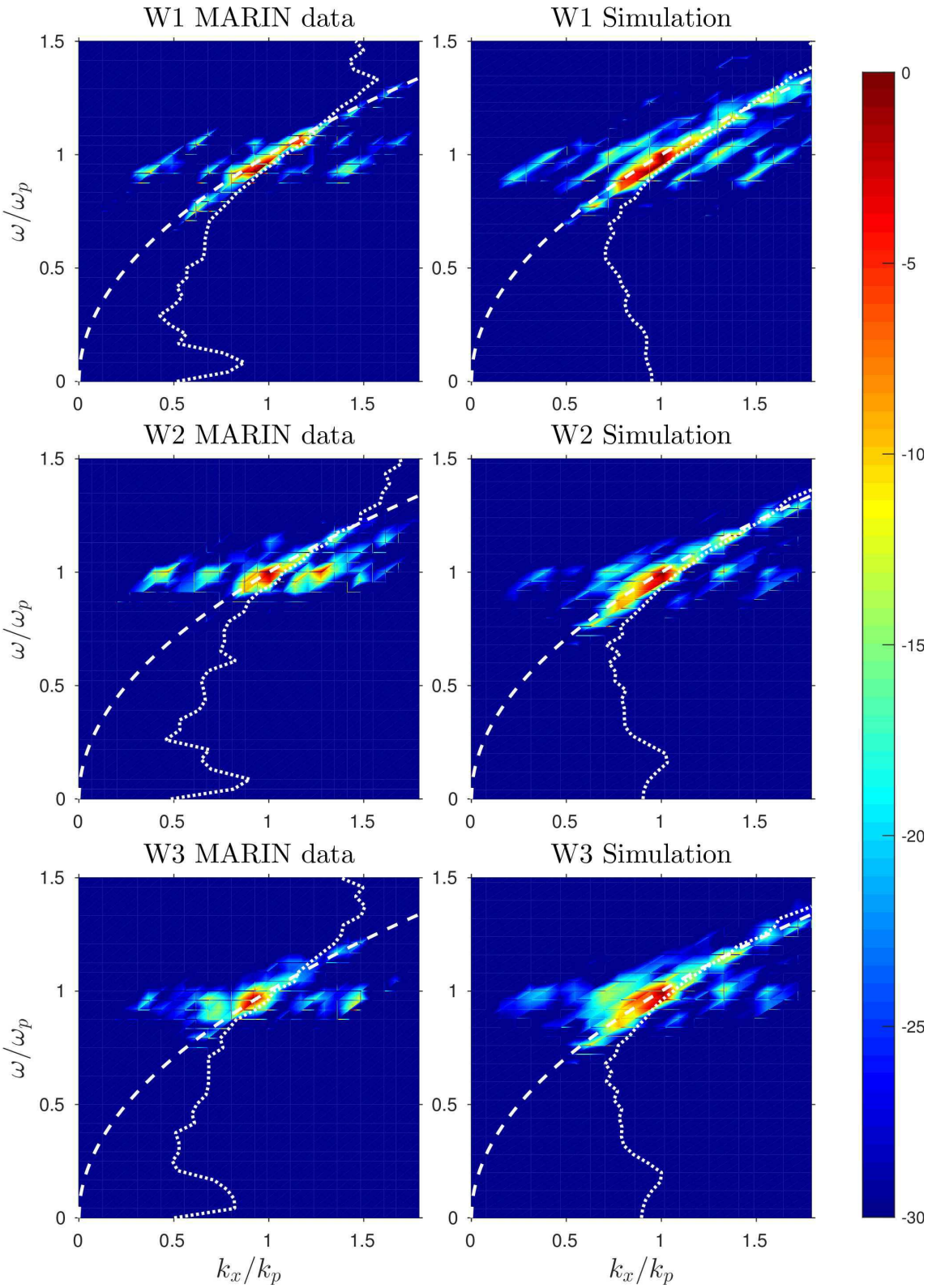

FIGURE 7. Left panes: (k_x, ω)-spectra obtained from sub-array 1 in the MARIN basin. Right panes: (k_x, ω)-spectra obtained from simulations of the MNLS equation. Colours: Spectral energy density in dB. Colour bar in dB. White dashed curve: (4.1). White dotted curves: RMS wavenumber k_{RMS} from (2.14).

Considering the group velocity $\mathbf{c_g}$ of the peak, the sub-domains were not affected by the periodic boundary conditions of the simulations. Waves leaving the sub-domains would propagate with $\mathbf{c_g}$ in the full domain without reaching the boundary of the sub-domain during the time of $50T_p$ used for the spectral estimates.

5. Discussion

A number of directional waves have been simulated with the NLS and MNLS equations for ranges of steepness and bandwidth. From the (k, ω)-spectra the deviation from LDR has been observed for narrow-banded directional waves.

For the NLS and MNLS equations the deviation is qualitatively different. The NLS equation shows deviation both above and below peak while the MNLS equation shows deviation only above peak. For the highest steepness the MNLS equation shows a more pronounced deviation above peak than the NLS equation during the $150T_p$ considered.

We performed simulations over longer times up to $200T_p$ which revealed that the narrow-banded directional waves eventually reach a quasi-stationary state with relaxation toward LDR. Our unidirectional waves show deviation during the entire time up to $200T_p$ and do not relax toward LDR. Thus, qualitative difference between directional and unidirectional wave propagation is observed.

In accordance with the BF timescale deviation occurs and relaxes sooner for directional waves with high steepness than for waves with lower steepness.

A proposed deviation parameter δ shows that the dispersion of the directional waves deviates from the LDR when BFI is high and crests are long. The magnitude of δ increases when BFI increases. The result is evident for all steepnesses considered.

For broad-banded steep waves the spectral energy density is distributed around $\omega(k + \Delta k) + \Delta\omega$, often used as the upper bound of radar filters above the LDR, where Δk and $\Delta\omega$ are the resolutions along the wavenumber and frequency axes. This may help to improve analysis of marine radar imagery where the filter is used to supress those spectral contributions that do not satisfy the LDR, see Nieto Borge *et al.* (2004).

The MARIN data confirms the simulations for three cases of BFI and L_c situated away from the highest values of the deviation parameter δ.

Considering ω_p, k_p and ϵ for the MARIN wave fields given in table 1, and BF timescale $\tau = (\epsilon^2\omega_p)^{-1}$, the characteristic distances are $c_g\tau \approx 77$ m for W1 and 84 m for W2 and W3. The length of the synthetic array along main wave direction in the MARIN basin, 25.6 m, does not cover the BF scale. The MARIN array covers 15–$16\lambda_p$ along main wave direction, considerably less than the $70\lambda_p$ of the simulations presented in §3 which cover the BF scale. We computed (k_x, ω)-spectra for directional waves with $\epsilon = 0.04$ using the Gaussian spectrum (2.7) with narrow bandwidths instead of the JONSWAP spectrum shown in the right panes of figure 7. These spectra showed deviation from LDR. The simulations have periodic boundary conditions, different from the basin where waves have finite time to evolve from the wave maker to the damping beach. From the simulations in §3 we have seen that deviation occurs late for low steepness within the $150T_p$ considered. A basin with sufficient coverage to capture the late occurence of deviation for low steepness required to reveal the deviation. Thus due to the combinations of relatively broad frequency bandwidths, short crests and limited spatial coverage it should not be expected that deviation due to nonlinear evolution should be observable from the MARIN data.

For unidirectional waves the deviation was observed experimentally and numerically by Taklo *et al.* (2015) and numerically by Gibson & Swan (2006), Krogstad & Trulsen (2010) and Houtani *et al.* (2015). The experiments of Taklo *et al.* (2015) employed $\epsilon = 0.10$

which is higher than $\epsilon = 0.04$ of the MARIN wave fields. The simulated unidirectional narrow-banded waves with $\epsilon = 0.04$ in §3 reveal deviation late during the time considered, similar to that of the directional waves shown in the upper right pane of figure 2. Thus a sufficiently long narrow wavetank could capture the deviation for low steepness.

6. Conclusion

We have examined the dependence of the dispersion of directional surface gravity waves on BFI and crest length. A parameter for describing the deviation between the dispersion of simulated waves and the theoretical linear dispersion relation has been proposed. The deviation is most pronounced when BFI is high and crests are long. The deviation increases when BFI increases. We have also considered laboratory data of directional waves from MARIN. The MARIN data confirms the simulations for three cases of BFI and crest length.

Acknowledgements We would like to acknowledge several useful comments by the referees. This research has been supported by the University of Oslo and the Research Council of Norway through grant 214556/F20. For the present study use has been made of the extensive two-dimensional wave measurements conducted by MARIN in Wageningen as part of the On Board Wave and Motion Estimator (OWME) JIP. The authors would like to thank MARIN and the participants in the OWME JIP (Gusto, Kongsberg, SBM, Seaflex, Sirehna, Statoil and Total) for making the data available for this study.

REFERENCES

Alber, I. A. 1978 The effects of randomness on the stability of two-dimensional surface wavetrains. *Proc. R. Soc. Lond. A.* **363**, 525–546.

Alber, I. A. & Saffman, P. G. 1978 Stability of random nonlinear deep water waves with finite bandwidth. *TWR Defense and Spacesystems Rep.* pp. 31326–6035–RU–00, 89.

Bateman, W. J. D., Swan, C. & Taylor, P. H. 2001 On the efficient numerical simulation of directionally-spread surface water waves. *J. Comput. Phys.* **174**, 277–305.

Crawford, D. R., Saffman, P. G. & Yuen, H. C. 1980 Evolution of a random inhomogeneous field of nonlinear deep-water gravity waves. *Wave Motion* **2**, 1–16.

Dysthe, K. B. 1979 Note on a modification to the nonlinear Schrödinger equation for application to deep water waves. *Philos. Trans. R. Soc. A.* **369**, 105–114.

Fessler, J. A. & Sutton, B. P. 2003 Nonuniform fast Fourier transform using min-max interpolation. *IEEE Transactions on Signal Processing* **51**, 560–574.

Gibson, R. S. & Swan, C. 2006 The evolution of large ocean waves: the role of local and rapid spectral changes. *Proc. R. Soc.* **463**, 21–48.

Goda, Y. 2000 *Random seas and design of maritime structures*. World Scientific, Singapore.

Gramstad, O. & Trulsen, K. 2007 Influence of crest and group length on the occurence of freak waves. *J. Fluid Mech.* **582**, 463–472.

Houtani, H., Waseda, T., Fujimoto, W., Kiyomatsu, K. & Tanizawa, K. 2015 Freak wave generation in a wave basin with HOSM-WG method. *In ASME 2015 34th Int. Conf. on Ocean, Offshore and Artic Eng. American Soc. of Mech. Engineers.* **V007T06A085**, 1–15.

Janssen, P. A. E. M. 2003 Nonlinear four-wave interactions and freak waves. *A. Met. Soc.* **33**, 863–884.

Krogstad, H. E. & Trulsen, K. 2010 Interpretations and observations of ocean wave spectra. *Ocean Dynamics* **60**, 973–991.

Lo, E. & Mei, C. C. 1985 A numerical study of water-wave modulations based on a higher-order nonlinear Schrödinger equation. *J. Fluid Mech.* **150**, 395–415.

Lo, E. & Mei, C. C. 1987 Slow evolution of nonlinear deep water waves in two horizontal directions: A numerical study. *Wave Motion* **9**, 245–259.

Mori, N., Onorato, M. & Janssen, P. A. E. M. 2011 On the estimation of the kurtosis in directional sea states for freak wave forecasting. *J. Phys. Oceanography* **41**, 1484–1497.

Naaijen, P., van Dijk, R., Huijsmans, R. H. M., El-Mouhandiz, A. A. & Danneberg, J. 2009 Real time estimation of ship motions in short crested seas. *Proc. OMAE* .

Nieto Borge, J. C., Rodr´iguez, G., Hessner, K. & Izquierdo, P. 2004 Inversion of marine radar images for surface wave analysis. *J. Atmos. Ocean Tech.* **21**, 1291–1300.

Onorato, M., Osborne, A. R., Serio, M. & Bertone, S. 2001 Freak waves in random oceanic sea states. *Phys. Rev. Letters* **86**, 5831–5834.

Simanesew, A., Krogstad, H. E., Trulsen, K. & Nieto Borge, J. C. 2016 Development of frequency-dependent ocean wave directional distributions. *Applied Ocean Research* **59**, 304–312.

Socquet-Juglard, H., Dysthe, K., Trulsen, K., Krogstad, H. E. & Liu, J. D. 2005 Probability distributions of surface gravity waves during spectral changes. *J. Fluid Mech.* **542**, 195–216.

Taklo, T. M. A., Trulsen, K., Gramstad, O., Krogstad, H. E. & Jensen, A. 2015 Measurement of the dispersion relation for random surface gravity waves. *J. Fluid Mech.* **766**, 326–336.

Toffoli, A., Gramstad, O., Trulsen, K., Monbaliu, J., Bitner-Gregersen, E. & Onorato, M. 2010 Evolution of weakly nonlinear random directional waves: laboratory experiments and numerical simulations. *J. Fluid Mech.* **664**, 313–336.

Trulsen, K., Kliakhandler, I., Dysthe, K. B. & Velarde, M. G. 2000 On weakly nonlinear modulation of waves on deep water. *Phys. Fluids* **12**, 2432–2437.

Tucker, M. J. & Pitt, E. G. 2001 *Waves in ocean engineering*. Elsevier Science & Technology, Oxford.

Waseda, T., Kinoshita, T. & Tamura, H. 2009 Evolution of a random directional wave and freak wave occurence. *A. Met. Soc.* **39**, 621–639.

Xiao, W., Liu, Y., Wu, G. & Yue, D. K. P. 2013 Rouge wave occurence and dynamics by direct simulations of nonlinear wave-field evolution. *J. Fluid Mech.* **720**, 357–392.

Zakharov, V. E. 1968 Stability of periodic waves of finite amplitude on the surface of a deep fluid. *J. Appl. Mech. Tech. Phys.* **9**, 190–194.